Ultrasonics 95 (2019) 79–94

Contents lists available at ScienceDirect

Ultrasonics

journal homepage: www.elsevier.com/locate/ultras

Design and kinematic analysis of a novel decoupled 3D ultrasonic elliptical vibration assisted cutting mechanism

Chen Zhang*, Yun Song

College of Mechanical and Electrical Engineering, Nanjing University of Aeronautics and Astronautics, 210016, China

ARTICLE INFO

Keywords:
3D ultrasonic EVC mechanism
Flexure hinge
Planar parallelogram joint
Decoupling analysis
Kinematic modelling
Displacement amplification
FEA simulation

ABSTRACT

The 3D elliptical vibration-assisted cutting (EVC) mechanism with arbitrary elliptical locus in space has a wide array of industrial applications for generating micro/nano-structured surface. However, the current 3D EVC mechanism are limited by their motion couplings, resonant frequencies and regulation of arbitrary elliptical locus. In order to improve the output properties, an innovative decoupled 3D ultrasonic EVC mechanism is proposed in the form of compliant parallel mechanism. First, the proposed 3D ultrasonic EVC mechanism is specifically designed to be capable of generating uniformly magnified output displacement in three directions and its 3D elliptical locus is obtained by the designed multi-axis flexure hinge structure with three orthogonal sub chains. Design process of multi-axis flexure hinge structure is respectively described from displacement amplification and decoupling output. The kinematics and amplification ratios of the designed 3D EVC mechanism are analytically modeled and a finite element analysis is performed to validate the designed 3D EVC mechanism. Based on the analysis results, a prototype device is fabricated, and then its vibration characteristics are evaluated by using the established test system. The test experiments show that the performance of the developed 3D ultrasonic EVC mechanism is satisfied.

1. Introduction

Elliptical vibration assisted cutting (EVC) is widely regarded as a potential process for the generation of micro/nano-structured surface with wavelengths above tens of microns and nanometric surface roughness. Since it adds small-amplitude, high-frequency tool displacement to the cutting motion of tool, which brings a lot of machining advantages, such as lower cutting forces, longer tool life, and better surface finish [1,2]. According to surface generation mechanism, micro/nano-structured surface can be generated by using the suitable EVC processes [3–9]. Zhang et al. [3] reviewed some detailed applications of the micro/nano structure fabrication by applying the different types of elliptical vibrators in EVC process. Zhu et al. [4,5] presents a novel two-dimensional vibration-assisted compliant cutting system (2-D VCCS) to be used on conventional machines for generating textured surfaces with uniform and accurate topography and further considered the theoretical analysis on the cutting force through both finite element and mechanistic analytical models to present a systematic investigation in the generation process of micro -structured surface by using fast-/slow tool servo (F-/STS) diamond turning. Zhu et al. [6] developed a novel 2-D vibration-assisted compliant cutting system for surface texturing. Suzuki et al. [7] proposed a new ultra-precision sculpturing method at the micro/nano scale for difficult-to-cut materials by utilizing the variations of the 2D elliptical vibration locus of the cutting tool while Zhang et al. [8] further explored ultra-precision nano-structure fabrication by the amplitude control sculpturing method in 2D elliptical vibration cutting considering locus compensation. Gandhi et al. [9] investigated the ability to prescribe micro-scale textures of controlled size and morphology by the control of the underlying process parameters in vibration/modulation-assisted machining.

Compared to the 2D EVC, the 3D EVC can generate arbitrary elliptical motion in 3D space, which can be used to machine sculptured surface [10]. Shamoto et al. firstly proposed a method of machining free-form surface by using 3D EVC [11]. Lin et al. [12] studied tool path generation method for fabricating optical freeform surface by non-resonant 3D EVC. In 3D EVC process, the output characteristic of 3D EVC mechanism, which is used to generate the elliptical motion in 3D space, is an important index of the 3D EVC mechanism. In order to generate the elliptical motion, piezo-actuated compliant mechanisms are predominantly adopted to achieve high resonant frequency as well as high stiffness [13,14]. Serial mechanisms and parallel mechanisms are two commonly forms of compliant mechanism. The applications of compliant serial mechanisms are limited by their output motions, stiffness,

* Corresponding author.
E-mail address: meeczhang@nuaa.edu.cn (C. Zhang).

https://doi.org/10.1016/j.ultras.2019.03.012
Received 21 September 2018; Received in revised form 13 February 2019; Accepted 13 March 2019
Available online 14 March 2019
0041-624X/

heat balance, repeatability and resonant frequencies, to mention a few. But compliant parallel mechanisms offer the possibility for the design of compact monolithic structures to generate uniformly magnified output properties in all directions and is widely used in the structure of EVC apparatus [15–17], positioning stage [18–20]. Hao [21] proposed the monolithic decoupled XYZ compliant parallel mechanisms (CPMs) for multi-function applications, which can be fabricated monolithically without assembly and has the capability of kinetostatic decoupling and Li et al. [22] introduces a screw theory based method termed constraint and position identification (CPI) approach to synthesize decoupled spatial translational compliant parallel manipulators (XYZ CPMs) with consideration of actuation isolation. These can provide the important theory foundation for the design of compliant parallel mechanism. The elliptical motion in 3D space can be obtained by using the compliant parallel mechanism. In order to use compliant mechanism in 3D EVC mechanism, it is required to obtain the tri-axial output motions and to to keep uniform magnification output in three directions. In its simplest form, the tri-axial output motions can be realized by serial structures which consist of three 1-DOF joints [23]. On the other hand, the tri-axial output motions can also be generated by parallel structures which consist of different sub chains to provide the connection between a fixed and a moving platform [24,25]. Compared to open-loop serial structures, closed-loop parallel structure can provide more constraints by the different sub chains combination to achieve higher output stiffness and higher resonant frequencies for 3D EVC apparatus. Motion decoupling is widely regarded as the most essential factor to guarantee motion accuracy and feedback control stability for 3D elliptical motion [20]. A novel piezo-actuated compliant mechanism is developed to obtain tri-axial translational motions with decoupled features for nano-cutting and open-loop test on the prototype shows that proper strokes with low coupling and high natural frequencies are obtained as estimated [26].

However, the current design of 3D EVC mechanism face two vital problems that have not addressed yet. First, a large number of compliant linkages and complicated structures are deliberately designed to isolate input motions, which may lead to low response speed induced by large moving inertia, as well as over-sized dimensions [18,27] in order to realize the motion decoupling and the commonly adopted assembly strategy of the complicated structures can induce undesired misalignment error and over-large motion loss in the flexural connections. Second, in a wide array of industrial applications, suitable ultrasonic resonant frequency, displacement amplification and the automated regulation of 3D elliptical vibration locus is also required to be considered in the topology and mechanical structures design of 3D EVC mechanism and little efforts are focused on the locus control of the elliptical vibration, which hinders the adaptability of the proposed 3D EVC mechanism. Also, decoupling, large output displacement and high resonant frequency are required on fabricating the free-from surface and complicated micro/nano textures for 3D EVC mechanism, e.g., rotary shafts with micro-texturing for reduced fluid resistance or friction. For such applications, it is necessary to understand the generation mechanism of 3D EVC locus and to design a decoupled compliant mechanism in three directions with certain amplification function for obtaining large output displacement. In this paper, a new decoupled 3D ultrasonic EVC mechanism is proposed in the form of a compliant parallel mechanism, and the design, decoupling analysis and kinematics modelling of compliant parallel mechanism and generation method of 3D elliptical vibration locus are studied systematically.

The paper is organized as follows. First, design of 3D ultrasonic EVC mechanism is given in Section 2. Section 2.1 describes the basic idea of design of 3D ultrasonic EVC mechanism. Section 2.2 introduces the conception design of the 3D ultrasonic EVC mechanism. Decoupling analysis of 3D ultrasonic EVC mechanism is described in Section 2.3. Section 2.4 is kinematic and amplification ratio modelling of 3D ultrasonic EVC mechanism. The geometric modelling and fabrication of 3D ultrasonic EVC mechanism are specifically described in Section 2.5. FEA simulation is used to validate the performance of 3D ultrasonic EVC mechanism in Section 3. The tests of the actual developed 3D ultrasonic EVC mechanism are conducted in Section 4. Conclusions are given in Section 5.

2. Design of 3D ultrasonic EVC mechanism

2.1. Basic idea of 3D EVC mechanism design

For obtaining the elliptical motion in 3D space, the common idea is to generate displacement output in three directions and three generated displacement outputs are combined into the elliptical locus. To generate displacement output in three directions, displacement output mechanism in each direction can be designed by exerting input displacement on each direction. Thus, the layout of three displacement output mechanisms is a key in the design of 3D ultrasonic EVC mechanism besides the design of displacement output mechanism.

In general, the orthogonal displacement output mechanisms in space can reduce the mutual influence of the output displacement in different direction and the output displacement in different direction is easy to combine together. At the same time, the orthogonal layout is convenient to machine for the specific structure. Based on the above advantages of orthogonal layout, the orthogonal layout of three displacement output mechanisms is selected. The schematic of orthogonal layout of three displacement output mechanisms is shown in the Fig. 1. In Fig. 1, three orthogonal input displacements will generate three orthogonal output displacements and three orthogonal output displacements will combine into an elliptical locus on output point.

Each displacement output structure in three directions forms a sub chain. For 3D ultrasonic EVC mechanism, the common output motions of three sub chains are three magnified translational outputs, which are required to be respectively generated by the three displacement amplification structures in each sub chain.

With the layout of three sub chains, the displacement amplification structure needs to be considered in the structural design of 3D ultrasonic EVC mechanism. In accordance with the motions of linkage mechanisms, the principles of mechanical displacement amplification can be categorized into several types such as lever amplification, triangular amplification, the bridge-type amplification, the Scott-Russell-type amplification, and the double-rocker-type amplification. In these types, lever amplification and triangular amplification are two basic amplification structure, which can be easily to connect with the designed original structures. The mechanical structures corresponding to these two principles of displacement amplification are depicted in Fig. 2.

For lever amplifier shown in Fig. 2(a), the rotation is used to generate the magnified output displacement. The magnified ratio of a lever amplifier can be obtained by analyzing the transform relationship of different links. The lengths of links O_1A and O_1B are l and l_1,

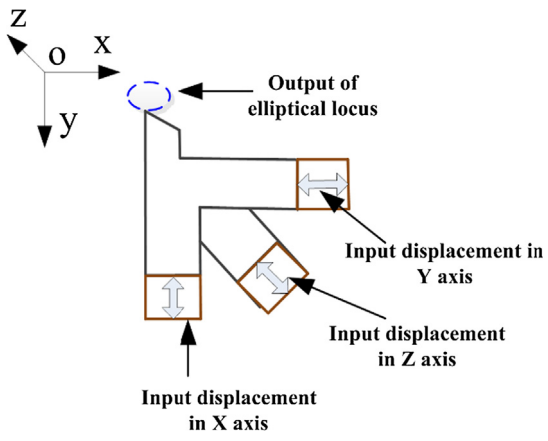

Fig. 1. The schematic of orthogonal layout of three sub chains.

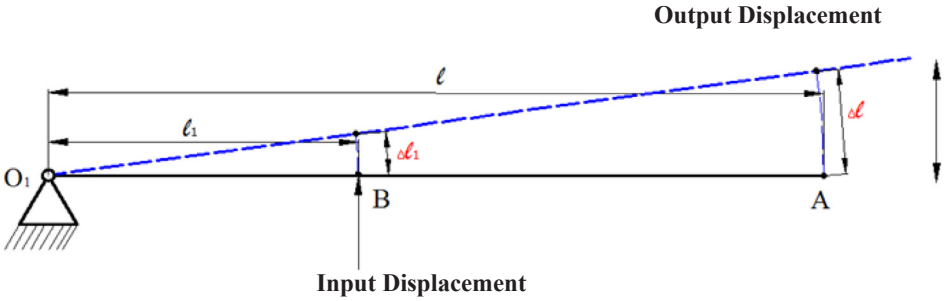

(a) Lever amplification

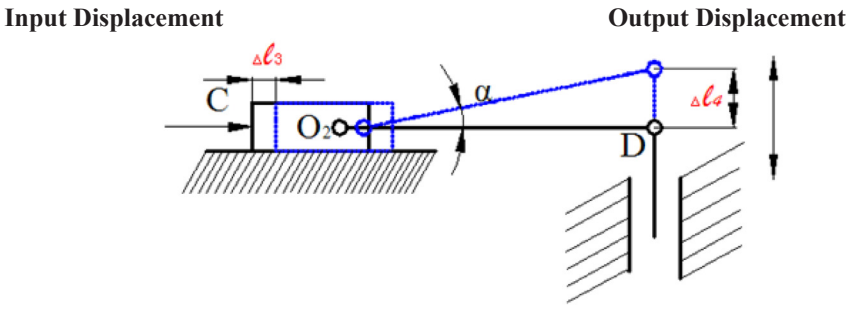

(b)Triangular amplification

Fig. 2. The principles of mechanical displacement amplification.

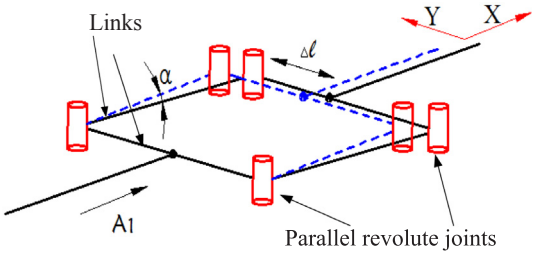

Fig. 3. Planar parallelogram joints.

respectively. The displacement Δl_1 of point B will generate output displacement Δl in point A. Thus, the amplification ratio k_1 of a lever amplifier can be obtained as:

$$k_1 = \frac{\Delta l}{\Delta l_1} = \frac{l}{l_1} \tag{1}$$

Fig. 2(b) shows a triangular amplifier and the magnified output displacement is a translational displacement Δl_4 along the point *D*. The instantaneous amplification ratio in triangular amplification can be determined as $k = cot\ (\alpha)$ based on instantaneous velocity analysis, where the intersection angle α should be less than $\pi/4$ to achieve the effect of output amplification.

The above two mechanical amplifications can be realized by a driven linkage which consists of two parallel revolute joints and a prismatic joint. The motions of the driven linkages can be represented by a planar displacement subset defined in terms of two translational displacements and a rotational displacement. In the displacement output structure, considering the compact structure and convenient use for fabricating micro/nano-structured surface, a triangular amplifier is selected. When selecting the layout form of output displacement structure for elliptical vibration locus generation and amplification structure, and then the displacement output structure in three directions can be designed based on the determined layout and amplification structure. The following is the details about the design of the 3D ultrasonic EVC mechanism.

2.2. The conception design of 3D ultrasonic EVC mechanism

Based on the desirable properties of flexure hinge and mechanical amplification principles, a 3-DOF parallel mechanism with flexure hinges is proposed for 3D ultrasonic EVC mechanism design by using three directly connected translational displacement amplification mechanisms. Because the basic mechanical displacement amplification is generated by the structure of a planar displacement subset, the planar displacement is used in the sub chains to generate the magnified translational outputs. Translational displacement output can be provided by a planar parallelogram joint, which is defined as a parallelogram consisting of four links that are connected by four parallel revolute joints shown in the Fig. 3. Based on the principle of triangular amplification in Fig. 2(b), the planar parallelogram joint can be used to generate translational displacement amplification according the triangle amplification principles. In Fig. 3, the input displacement in X axis will obtain the amplified output displacement in Y axis. Compared with other types of flexure hinges, circular flexure hinge with right cross-section has higher motion precision for rotational accuracy and is the optimal choice of the revolute joint in Fig. 3.

The planar parallelogram joint can be used to generate translational displacement amplification in different directions when the planar parallelogram joint is placed along different directions in fixed reference frame. The translational displacement output with amplification can be obtained shown in Fig. 4(a) and (b) by placing the parallelogram joints along Y axis and Z axis. Each planar parallelogram joint uses the same structure in Fig. 4(a) and (b) and is also a flexure hinge unit. In Fig. 4(a), the output displacement is along Y axis direction and the planar parallelogram joint is named as flexure hinge unit along Y axis. In Fig. 4(b), the output displacement is along Z axis direction and the planar parallelogram joint is named as flexure hinge unit along Z axis. With combining flexure hinge unit along Y axis and flexure hinge

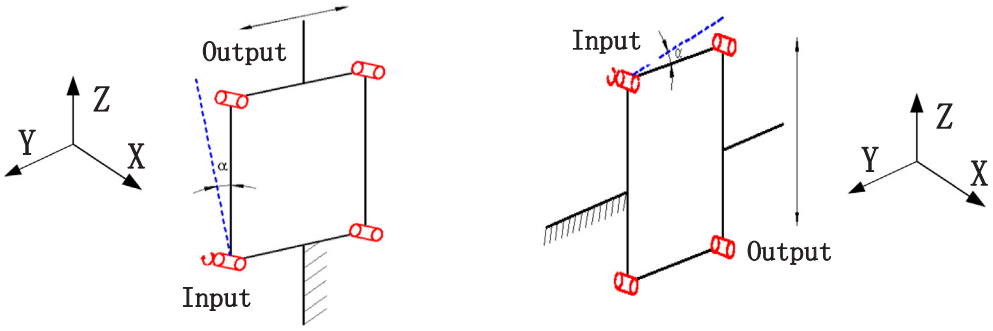

(a) Flexure hinge unit along Y axis (b) Flexure hinge unit along Z axis

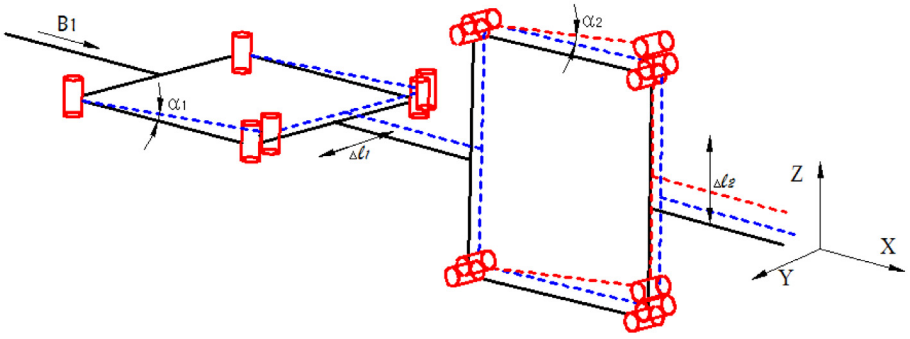

(c) The schematic of sub chain along X axis

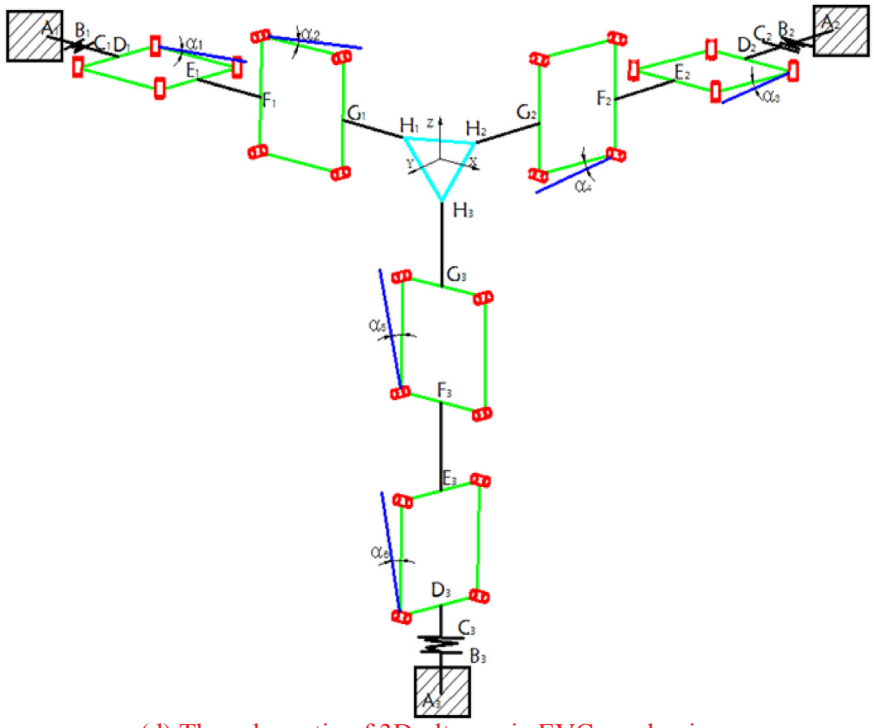

(d) The schematic of 3D ultrasonic EVC mechanism

Fig. 4. The design process of 3D ultrasonic EVC mechanism.

unit along Z axis in the orthogonal direction, one displacement output structure along X axis direction is constructed shown in Fig. 4(c). The designed displacement output structure along X axis direction is named as sub chain along X axis and can output the displacement along Y axis and Z axis. Using the same way, one displacement output structure along Y axis direction is established by combining flexure hinge unit along Z axis and flexure hinge unit along X axis in the orthogonal direction and one displacement output structure along Z axis direction is

obtained by combining flexure hinge unit along X axis and flexure hinge unit along Y axis in the orthogonal direction.

Three sub chains along X axis, Y axis and Z axis with the same two planar parallelogram joints is respectively constructed based on the above method and three sub chains are connected with the common output point (moving platform) based on the orthogonal layout. Each sub chain is connected with a translational displacement input unit to provide the input displacement. Thus, a multi-axis flexure hinge structure is formed by placing three sub chains in an orthogonal form shown in Fig. 4(d). By adding the corresponding piezoelectric actuators in each sub chain, fixed frame and moving frame (the common output point of three sub chains) on the designed multi-axis flexure hinge structure, the 3D ultrasonic EVC mechanism can be obtained to generate the elliptical locus in 3D space.

In established 3D ultrasonic EVC mechanism, three magnified translational outputs along the three axial directions X, Y, Z in sub chain along X axis can be generated by exerting the input planar displacement of A1, A2 and A3 respectively in three axial directions X, Y, Z shown in Fig. 4(d). The instantaneous amplification ratios of the sub chain along X axis in the three directions X, Y, Z are respectively 1, cot (α_1) and cot (α_2) shown in Fig. 4(d). Correspondingly, the instantaneous amplification ratios of the sub chain along Y axis along the three directions X, Y, Z are respectively cot (α_3), 1 and cot (α_4) and the instantaneous amplification ratios of the sub chain along Z axis in the three directions X, Y, Z are respectively cot (α_5), cot (α_6) and 1. Three same sub chains, which is perpendicular to each other, are connected to generate the magnified displacement output in three directions.

2.3. Decoupling analysis of 3D EVC mechanism

In the orthogonal form of the parallel displacement amplifier, the structure can be analyzed based on the one translational displacement input unit and two flexure hinge units with amplification in each sub chain shown in Fig. 4(d). The translational displacement input unit can be considered as the independent active motions, while the flexure hinge units with amplification structure are dependent passive motions concerning the connections between the moving platform and the three sub chains. The motion of the flexure hinge units with amplification structure are induced by the translational displacement input unit. For each sub chain in the multi-axis flexure hinge structure, the motions of two flexure hinge units with amplification structure are not independent. That means that the motions of two flexure hinge units with amplification structure in each sub chain are dependent motions, which concerns the other two sub chains and the connections between the moving platform and the three sub chains. The motions of each sub chain is from the translational displacement input unit and the translational displacement input unit is feed by the piezoelectric actuator. Based on the initial position of the structure in Fig. 4(d), three translational displacements input of each sub chain are generated by the piezoelectric actuator. The output displacement of moving platform along the X axis, Y axis and Z axis in multi-axis flexure hinge structure can be obtained by the exerting input displacements. Simultaneously, the translational output displacements of moving platform along the X axis, Y axis and Z axis are not only dependent on the three translational input displacements, but are also, correspondingly, affected by two flexure hinge units with amplification structure in each sub chain.

In order to understand the decoupling properties of 3D ultrasonic EVC mechanism, it needs to analyze the influence of each sub chain with input displacement on other sub chain. Supposed the input displacements of three sub chains are Δs_1, Δs_2 and Δs_3, and the output displacements of moving frame are Δl_1, Δl_2 and Δl_3, and the lengths of the first sub chain, the second sub chain and the third sub chain between the moving platform and the fixed platform in 3D EVC mechanism are respectively D_1, D_2 and D_3 shown in Fig. 5. The generated displacement of the second sub chain induced by the first sub chain

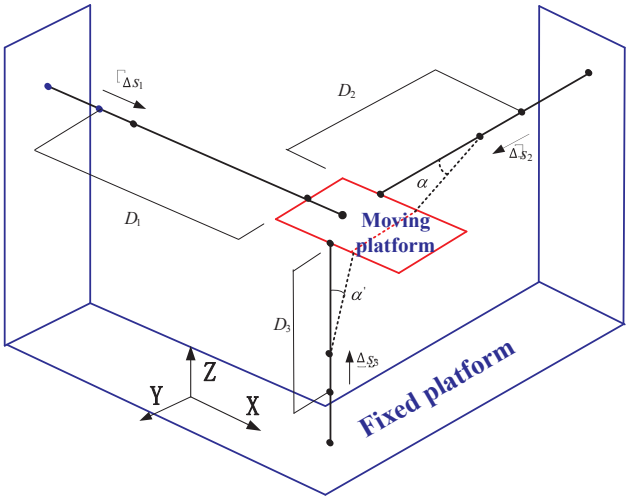

Fig. 5. The decoupling analysis schematic of 3D ultrasonic EVC mechanism.

under input displacement Δs_1 is Δs_{12}. According to the existing triangular amplification relationship, Δs_{12} can be expressed as $\Delta s_{12} = \frac{\Delta s_1}{\cot(\alpha)}$. The angle$\alpha$ is a rotation angle of the second sub chain induced by the first amplification unit of the first subchain with the input displacement Δs_1 and is equal to $\arctan\left(\frac{\Delta s_1}{D_2}\right)$.

Thus, the Δs_{12} can be further simplified as:

$$\Delta s_{12} = \frac{(\Delta s_1)^2}{D_2} \tag{2}$$

The input displacement Δs_1, which is from the piezoelectric actuator, is very small (e.g., from 2 μm to 20 μm) compared to D_2, and the length of the second sub chain D_2 is 28 mm in the design. The intersection angles in the second sub chain will be relatively small from 0.004° to 0.04°. By substituting the input displacement Δs_1 and the intersectional angle α into the Eq.(2), the Δs_{12} becomes relatively tiny such as from 0.00014 μm to 0.014 μm compared to the input displacement Δs_1. The effect of Δs_{12} compared to that of input displacement Δs_1, Δs_2 and Δs_3 on the output displacement Δl_1, Δl_2 and Δl_3 can be ignored. The same analysis is also applied in the second subchain and the third subchain and the similar results can be obtained for the second subchain and the third subchain because the second sub chain and the third sub chain have the same structure with the first sub chain. Thus the three orthogonal input displacement in three sub chains can be approximately considered as the decoupled motions with the current input displacement generated by piezoelectric actuator. This shows that the designed 3D ultrasonic EVC mechanism with multi-axis flexure hinge structure in the paper is a decoupled mechanism in three orthogonal directions and can realize the decoupled functions.

2.4. Kinematic modelling of 3D ultrasonic EVC mechanism

As previously mentioned, from the kinematics point of view, the selected right circular flexure hinge can generate rotation about one axis, and is modelled as an ideal revolute joint. This indicates that the offset of revolute center during the motion of the relative links is not taken into consideration. During the kinematic analysis, the stiffness of the flexure hinges is also neglected. Thus, the pseudo-rigid-body model of multi-axis flexure hinge structure for 3D EVC mechanism is developed and shown in Fig. 6.

As shown in Fig. 6, s_i, (i = 1, 2, 3) denotes the input variables of the piezoelectric actuator a_i in three directions for multi-axis flexure hinge mechanism (subscript i = 1,2,3, represents the sub chain 1, 2 and 3 respectively). The initial input displacements in three directions are Δs_i(i = 1, 2, 3). A fixed coordinate frame O-XYZ is established with the origin located at the center of the fixed platform and the X axis is

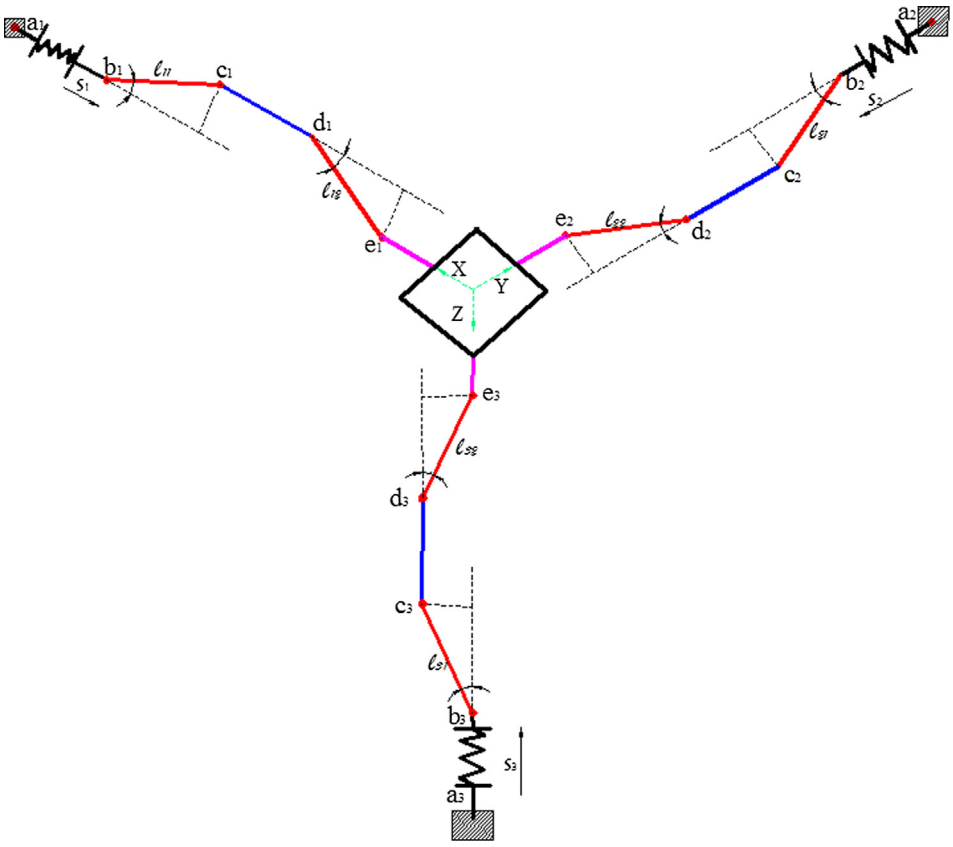

Fig. 6. Kinematics modelling schematic of multi-axis flexure hinge structure.

parallel to the sub chain 1 and the Y axis is parallel to the sub chain 2 and the Z axis is parallel to the sub chain 3. The moving coordinate frame $O' - x'y'z'$ is established with the origin located at the center of the moving frame and the x′ axis is parallel to the sub chain 1 and the y′ axis is parallel to the sub chain 2 and the z′ axis is parallel to the sub chain 3. The output variables of the moving frame are Δx, Δy and Δz in fixed coordinate frame O-XYZ. Under initial input displacements Δs_1 of the sub chain 1 along X axis, the generated displacements of two planar parallelogram joints are Δx_1 and Δy_1 and the rotational angles of two planar parallelogram joints are $\Delta\alpha_1$ and $\Delta\alpha_2$. The generated displacements of two planar parallelogram joints are Δy_2 and Δz_2 and the rotational angles of two planar parallelogram joints are $\Delta\alpha_3$ and $\Delta\alpha_4$ under initial input displacements Δs_2 of the sub chain 2 along Y axis. The generated displacements of two planar parallelogram joints are Δz_3 and Δx_3 and the rotational angles of two planar parallelogram joints are $\Delta\alpha_5$ and $\Delta\alpha_6$ under initial input displacements Δs_3 of the sub chain 3 along Z axis. The output displacements of the moving frame are $\Delta x'$, $\Delta y'$ and $\Delta z'$. Based on the connection relationship of the monolithic structure of multi-axis flexure hinge, the relationships among displacements Δx, Δy, Δz, Δx_1, Δy_1, Δy_2, Δz_2, Δz_3 and Δx_3 can be defined as:

$$\begin{cases} \Delta x = \Delta x_1 = \Delta x_3 \\ \Delta y = \Delta y_1 = \Delta y_2 \\ \Delta z = \Delta z_2 = \Delta z_3 \end{cases} \tag{3}$$

Three sub chains have the same structure and size in multi-axis flexure hinge mechanism and the rotational angle is very small. Supposed $l_{11} = l_{12} = l_{21} = l_{22} = l_{31} = l_{32} = l$ in Fig. 5, thus the rotation angles can be defined as:

$$\begin{cases} \Delta\alpha_1 = \Delta\alpha_6 = \sin\Delta\alpha_1 = \frac{\Delta x}{l} \\ \Delta\alpha_2 = \Delta\alpha_3 = \sin\Delta\alpha_2 = \frac{\Delta y}{l} \\ \Delta\alpha_4 = \Delta\alpha_5 = \sin\Delta\alpha_3 = \frac{\Delta z}{l} \end{cases} \tag{4}$$

Based on the energy conservation law, the relationships among driving forces, bending moments, the stiffness of flexure hinge and the rotational angles can be obtained as:

$$\begin{cases} F_1\Delta s_1 = 2M_1\Delta\alpha_1 + 2M_2\Delta\alpha_2 = 2K_1\Delta\alpha_1^2 + 2K_2\Delta\alpha_2^2 \\ F_2\Delta s_2 = 2M_3\Delta\alpha_3 + 2M_4\Delta\alpha_4 = 2K_3\Delta\alpha_3^2 + 2K_4\Delta\alpha_4^2 \\ F_3\Delta s_3 = 2M_5\Delta\alpha_5 + 2M_6\Delta\alpha_6 = 2K_5\Delta\alpha_5^2 + 2K_6\Delta\alpha_6^2 \end{cases} \tag{5}$$

where F_i, $(i = 1, 2, 3)$ denotes the driving force along X, Y and Z axis directions in multi-axis flexure hinge structure; M_i, $(i = 1, 2)$ expresses the bending moments of other two directions besides the input direction s_1 shown in Fig. 6; M_j, $(j = 3, 4)$ represents the bending moments of other two directions besides the input direction s_2 shown in Fig. 6; M_k, $(k = 5, 6)$ denotes the bending moments of other two directions besides the input direction s_3 shown in Fig. 6; K_i, $(i = 1, 2)$ are the stiffness of flexure hinge in other two directions besides the input direction s_1 shown in Fig. 6; K_j, $(j = 3, 4)$ are the stiffness of flexure hinge in other two directions besides the input direction s_2 shown in Fig. 6; K_k, $(k = 5, 6)$ are the stiffness of flexure hinge in other two directions besides the input direction s_3 shown in Fig. 6.

Substituting the Eq. (4) into the Eq. (5), the energy conservation law for multi-axis flexure hinge structure can be expressed as:

$$\begin{cases} F_1\Delta s_1 l^2 = 2K_1\Delta x^2 + 2K_2\Delta y^2 \\ F_2\Delta s_2 l^2 = 2K_3\Delta y^2 + 2K_4\Delta z^2 \\ F_3\Delta s_3 l^2 = 2K_5\Delta z^2 + 2K_6\Delta x^2 \end{cases} \tag{6}$$

Based on the Eq. (6), the output displacement Δx, Δy and Δz can be obtained as:

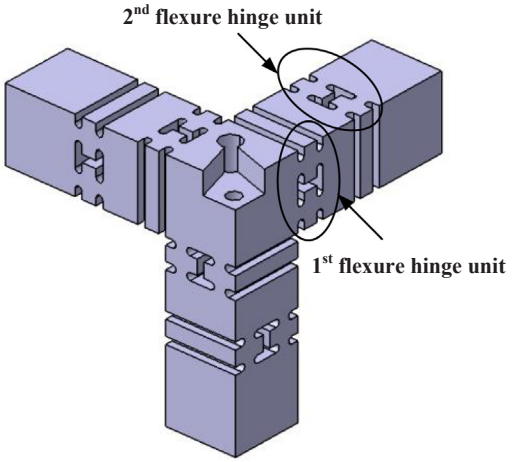

(a) The model of multi-axis flexure hinge structure

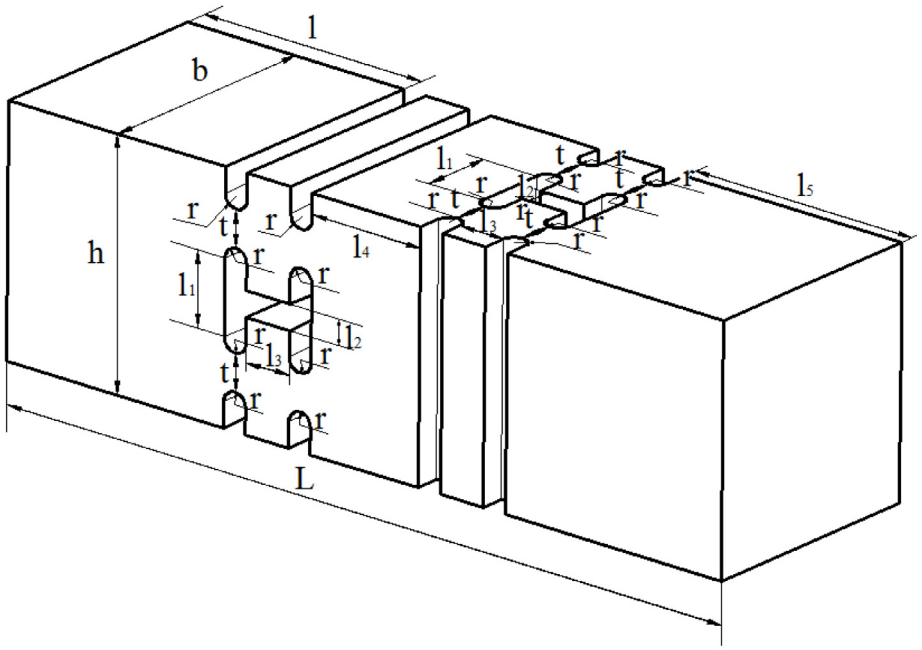

(b) The structural parameters of sub chain

Fig. 7. The schematic of multi-axis flexure hinge structure.

$$\begin{cases} \Delta x = l\sqrt{\dfrac{(K_3K_5F_1\Delta s_1 + K_2K_4F_3\Delta s_3 - K_2K_5F_2\Delta s_2)}{2K_1K_3K_5 + 2K_2K_4K_6}} \\ \Delta y = l\sqrt{\dfrac{(K_1K_5F_2\Delta s_2 + K_4K_6F_1\Delta s_1 - K_1K_4F_3\Delta s_3)}{2K_1K_3K_5 + 2K_2K_4K_6}} \\ \Delta z = l\sqrt{\dfrac{(K_2K_3F_2\Delta s_3 + K_1K_3F_3\Delta s_3 - K_3K_6F_1\Delta s_1)}{2K_1K_3K_5 + 2K_2K_4K_6}} \end{cases} \tag{7}$$

Thus, the amplification ratios k_x, k_y and k_z in X axis, Y axis and Z axis can be calculated as:

$$\begin{cases} k_x = (\Delta x + \Delta s_1)/\Delta s_1 = \dfrac{l}{\Delta s_1}\sqrt{\dfrac{(K_3K_5F_1\Delta s_1 + K_2K_4F_3\Delta s_3 - K_2K_5F_2\Delta s_2)}{2K_1K_3K_5 + 2K_2K_4K_6}} + 1 \\ k_y = (\Delta y + \Delta s_2)/\Delta s_2 = \dfrac{l}{\Delta s_2}\sqrt{\dfrac{(K_1K_5F_2\Delta s_2 + K_4K_6F_1\Delta s_1 - K_1K_4F_3\Delta s_3)}{2K_1K_3K_5 + 2K_2K_4K_6}} + 1 \\ k_z = (\Delta z + \Delta s_3)/\Delta s_3 = \dfrac{l}{\Delta s_3}\sqrt{\dfrac{(K_2K_3F_2\Delta s_3 + K_1K_3F_3\Delta s_3 - K_3K_6F_1\Delta s_1)}{2K_1K_3K_5 + 2K_2K_4K_6}} + 1 \end{cases} \tag{8}$$

In the designed multi-axis flexure hinge structure, three sub chains have the same structure and each sub chain includes two group of the same planar parallelogram joints. All planar parallelogram joints in multi-axis flexure hinge structure have the same structure and stiffness K. Thus, the following equation can be obtained as:

$$K_1 = K_2 = K_3 = K_4 = K_5 = K_6 = K \tag{9}$$

By substituting the Eq. (9) into the Eq. (7), the Eq. (7) can be further simplified as:

$$\begin{cases} \Delta x^2 = \dfrac{l^2(F_1\Delta s_1 + F_3\Delta s_3 - F_2\Delta s_2)}{4K} \\ \Delta y^2 = \dfrac{l^2(F_2\Delta s_2 + F_1\Delta s_1 - F_3\Delta s_3)}{4K} \\ \Delta z^2 = \dfrac{l^2(F_2\Delta s_3 + F_3\Delta s_3 - F_1\Delta s_1)}{4K} \end{cases} \tag{10}$$

Table 1
The values of structural parameter values of sub chain.

Parameter	Value/mm	Parameter	Value/mm	Parameter	Value/mm
L	35	b	10	h	10
r	0.5	l	10	t	1.5
l_1	3	l_2	1	l_3	3
l_4	5	l_5	10		

In order to obtain the output displacement in X axis, Y axis and Z axis, the same three piezo actuator are used to drive the designed multi-axis flexure hinge structure by exerting input displacement on X axis, Y axis and Z axis. Thus, the variances of the input displacement in three directions have the same value, that means $\Delta s_1 = \Delta s_2 = \Delta s_3 = \Delta s$. By substituting $\Delta s_1 = \Delta s_2 = \Delta s_3 = \Delta s$ into the Eq. (10), the Eq. (10) can be further simplified as:

$$\begin{cases} \Delta x^2 = \frac{l^2 \Delta s(F_1 + F_3 - F_2)}{4K} \\ \Delta y^2 = \frac{l^2 \Delta s(F_2 + F_1 - F_3)}{4K} \\ \Delta z^2 = \frac{l^2 \Delta s(F_2 + F_3 - F_1)}{4K} \end{cases} \tag{11}$$

If the stiffness of piezoelectric actuator is k, the driving force F can be expressed as:

$$F = k\Delta s \tag{12}$$

By substituting the Eq. (12) into the Eq. (11) the output displacement Δx, Δy and Δz can be obtained as:

$$\begin{cases} \Delta x = \frac{l\Delta s}{2}\sqrt{\frac{k}{K}} \\ \Delta y = \frac{l\Delta s}{2}\sqrt{\frac{k}{K}} \\ \Delta z = \frac{l\Delta s}{2}\sqrt{\frac{k}{K}} \end{cases} \tag{13}$$

The final output displacements $\Delta x'$, $\Delta y'$ and $\Delta z'$ along X axis, Y axis and Z axis in the coordinate system *O-XYZ* is equal to the sum of input displacement and the generated output displacement induced by other two sub chains and can be expressed as:

$$\begin{cases} \Delta x' = \Delta x + \Delta s = \frac{l\Delta s}{2}\sqrt{\frac{k}{K}} + \Delta s \\ \Delta y' = \Delta y + \Delta s = \frac{l\Delta s}{2}\sqrt{\frac{k}{K}} + \Delta s \\ \Delta z' = \Delta z + \Delta s = \frac{l\Delta s}{2}\sqrt{\frac{k}{K}} + \Delta s \end{cases} \tag{14}$$

Thus the amplification ratios k_x, k_y and k_z in X axis, Y axis and Z axis of 3D EVC mechanism can be written as:

$$\begin{cases} k_x = \left(\frac{l\Delta s}{2}\sqrt{\frac{k}{K}} + \Delta s\right)/\Delta s = \frac{l}{2}\sqrt{\frac{k}{K}} + 1 \\ k_y = \left(\frac{l\Delta s}{2}\sqrt{\frac{k}{K}} + \Delta s\right)/\Delta s = \frac{l}{2}\sqrt{\frac{k}{K}} + 1 \\ k_z = \left(\frac{l\Delta s}{2}\sqrt{\frac{k}{K}} + \Delta s\right)/\Delta s = \frac{l}{2}\sqrt{\frac{k}{K}} + 1 \end{cases} \tag{15}$$

From the Eq. (15), it can be concluded that the amplification ratios of 3D EVC mechanism in three directions is more than one at least and is related to the stiffness of piezoelectric actuators, the stiffness and link length of planar parallelogram joint in sub chains. The suitable amplification ration can be initially estimated based on the Eq. (15) in the design process of 3D EVC mechanism.

2.5. The geometric modelling and fabrication of 3D ultrasonic EVC mechanism

Based on the above conceptual design of the 3D EVC mechanism and kinematic modelling, a 3D ultrasonic EVC mechanism with flexure hinges was designed and realized. Three orthogonal sub chains form a multi-axis flexure hinge structure, which is illustrated in Fig. 7(a). The multi-axis flexure hinge structure is a 3-DOF parallel mechanism and includes three sub chains along X axis, Y axis and Z axis, and each sub chain is composed of two flexure hinge units. The first flexure hinge unit and the second flexure hinge unit in each sub chain are perpendicularly fabricated shown in Fig. 7(a). Thus, 3D output motions along X axis, Y axis and Z axis can be generated by the designed multi-axis flexure hinge structure and will generate the elliptical locus in 3D space. Thus, the design of multi-axis flexure hinge structure is a key in the 3D ultrasonic EVC mechanism. The main structural parameters of the designed sub chain are shown in Fig. 7(b) and three sub chains have the same structural parameters for multi-axis flexure hinge structure. The design of multi-axis flexure hinge structure adopts a compact structure with a uniform three sub chain. The corresponding value of structural parameters in Fig. 7(b) are listed in Table 1.

From the designed structural parameters of 3D ultrasonic EVC mechanism, the amplification ratio of 3D ultrasonic EVC mechanism can be calculated based on the Eq. (15). In Eq. (15), the stiffness of piezoelectric actuators is related to the section areas, the length and compliance coefficient of piezoelectric chip and can be calculated based on the selected piezoelectric chip in 3D ultrasonic EVC mechanism. The stiffness of piezoelectric actuators is expressed as:

$$k = A/(S_{33} * L_0) \tag{16}$$

where k is the stiffness of piezoelectric actuators, A is section area of piezoelectric chip, L_0 is length of piezoelectric chip, S_{33} is compliance coefficient of piezoelectric chip.

The inner diameter, outer diameter and length of the selected piezoelectric chip are respectively 5 mm, 10 mm and 4 mm. Based on the Eq.(16), the calculated stiffness of piezoelectric actuators is 987 N/μm and the stiffness of flexure hinge can be obtained according to the designed flexure hinge shown in Fig. 7. The stiffness of flexure hinge is 424 N/μm and the length of link is 5 mm show in Fig. 5 and Table 1. Thus, the amplification ratios k_x, k_y and k_z in X axis, Y axis and Z axis of 3D EVC mechanism can be calculated as: $k_x = k_y = k_z = 4.814$.

Based on the designed multi-axis flexure hinge structure, the 3D ultrasonic EVC mechanism can be established by adding the corresponding support component. The established geometric model of the 3D ultrasonic EVC mechanism is shown in Fig. 8 and is composed of the multi-axis flexure hinge structure, three piezo-actuators, three preload and adjustable bi-nut structures, fixed platform and moving frame (cutter setup frame). The multi-axis flexure hinge structure, as discussed above, mainly includes three sub chains along X axis, Y axis and Z axis and is used to support the moving frame (cutter setup frame) and pass the 3D elliptical motions to the moving frame. The 3D elliptical motions of moving frame drive the cutter move along the elliptical

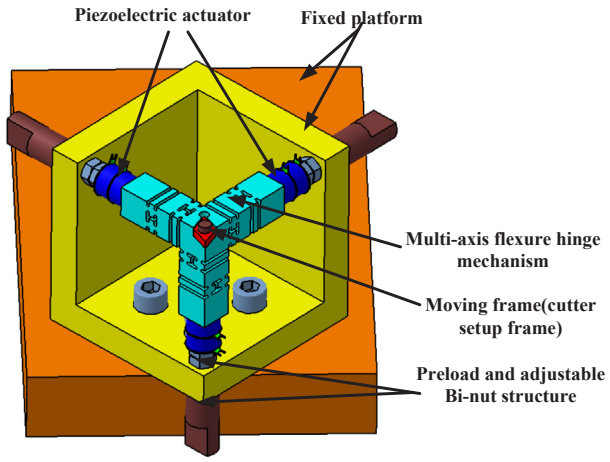

Fig. 8. The geometric model of 3D ultrasonic EVC mechanism.

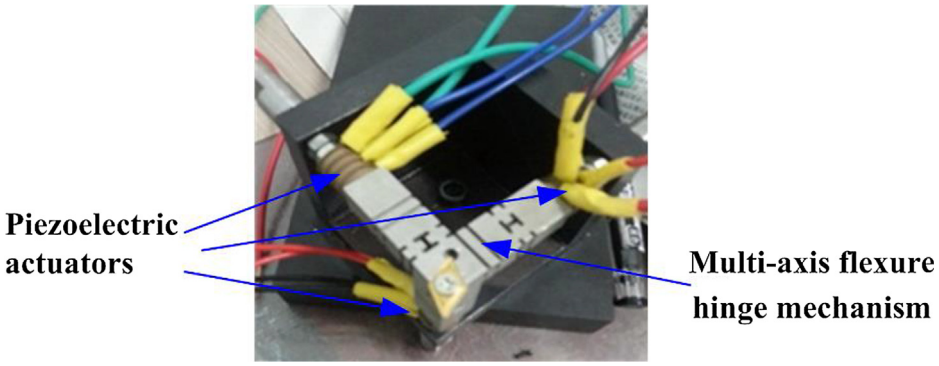

Fig. 9. The schematic of 3D ultrasonic EVC mechanism.

locus. In order to maintain the contact condition during the motion of such mechanisms, a suitable preload is necessary for the piezoelectric actuator. The bi-nut structures are designed to fix, preload and adjust the distance between piezoelectric chip and bi-nut. Thus the uniform and stable expansion and retraction can be generated by the piezoelectric chip. The magnitude of preload can be set by adjusting the bi-nut structures to avoid the bending and torsional movements acting at the piezoelectric actuator. A fixed platform is connected with multi-axis flexure hinge structure by using three preloads and adjustable bi-nut structures.

Based on the above geometric model of 3D ultrasonic EVC mechanism, a prototype device, as shown in Fig. 9, is fabricated. Fig. 9 shows the illustration of 3D ultrasonic EVC apparatus by replacing the revolute joints by right circular flexure hinges of the same dimension in three directions. Linear input motions for the 3D ultrasonic EVC apparatus is obtained by using the piezoelectric actuators. The multi-axis flexure hinge mechanism in 3D ultrasonic EVC mechanism can be fabricated by a standard EDM wire cutting machine. The fabricated multi-axis flexure hinge mechanism and piezoelectric actuator in three direction is also showed in Fig. 9.

3. FEA simulation of the 3D ultrasonic EVC mechanism

3.1. Mesh generation

To further examine the static and dynamic characteristics of the proposed 3D ultrasonic EVC mechanism, finite element analysis is conducted to perform static and dynamic investigation. FEA simulation results are utilized to calibrate the established model of 3D ultrasonic EVC mechanism. Based on the geometric model (Fig. 8), a finite element model for the designed 3D ultrasonic EVC mechanism is established and shown in Fig. 10. A SOLID227 element is utilized to mesh the flexure-based 3D ultrasonic EVC mechanism and three spring elements are used to simulate the effects of the equivalent driving stiffness of the piezoelectric actuators. The boundary conditions for finite element model are set up that the fixed platform is fixed and constrained for all degrees of freedom. Material parameters input to the simulation are material density 2700 kg/m^3 (aluminium alloy), Young's modulus 71.7 GPa and Poisson's ratio 0.33. The Block Lanczos method is adopted to extract the vibration mode shapes and the resonance frequencies in analysis process of the static and dynamic characteristic of 3D ultrasonic EVC mechanism. During the modal analysis, SOLID227 element is used for the meshing, and the voltages applied on the nodes of electrodes are set as zero. The tool, electrodes and glue layers were ignored, and the errors are acceptable. The PZT ceramics material is PZT-8 provided by Bao Dding HengSheng Acoustics Electron Apparatus Co., Ltd. in China.

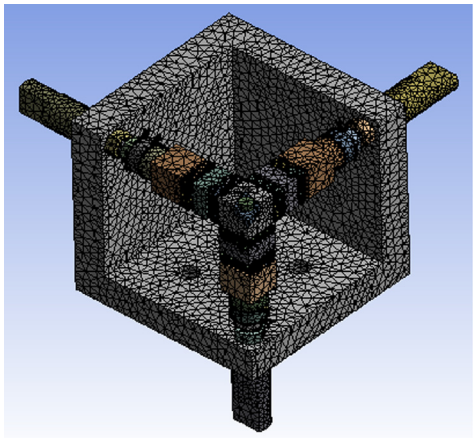

Fig. 10. Finite element model of 3D ultrasonic EVC mechanism.

3.2. Simulation process of 3D ultrasonic EVC mechanism

In the simulation, zero displacements are applied to the fixed platform in each sub chain for the frequency and static analysis. The input displacements are assumed to be 5 μm as provided by the piezoelectric actuator. The corresponding output displacements are extracted for the analyses of the frequency responses and displacement amplifications of finite element model of 3D ultrasonic EVC mechanism. The stress on the flexure hinges were also verified to avoiding fracture during operation. In general, the maximal cutting force exerting on the 3D ultrasonic EVC mechanism is 500 N according to the actual micro/nano-structured surface and the established finite element model shown in Fig. 10 is simulated. The simulation results about static analysis of 3D ultrasonic EVC mechanism are shown in Fig. 11. It can be seen that the maximum deflection and strain of the 3D EVC mechanism are 5.25 μm and 0.23 μm/mm respectively. The maximal stress is 45.7 MPa and is within the permissible stress range for aluminium alloy. Thus, the designed 3D ultrasonic EVC mechanism is safe.

In order to identify the resonant frequencies of 3D ultrasonic EVC mechanism, the calibration of resonant frequency by using harmonic responses is an important task in the design of 3D ultrasonic EVC mechanism. The harmonic responses are also evaluated by using the established finite element model by the method of mode suppression under the same conditions (material, constrains, loads and grid meshing) for the static analysis. The amplitudes of sinusoidal excitation signals applied on the PZT in harmonic responses are 350 V with a 0° phase difference between the signals; and the frequency is swept from 0 to 60 kHz with a step size of 200 Hz. For convenience of comparison, the amplitudes with FEA simulation in the three directions are shown in Fig. 12.

From the Fig. 12, it can be seen that the frequency responses in the three directions are slightly different while the resonant frequencies are

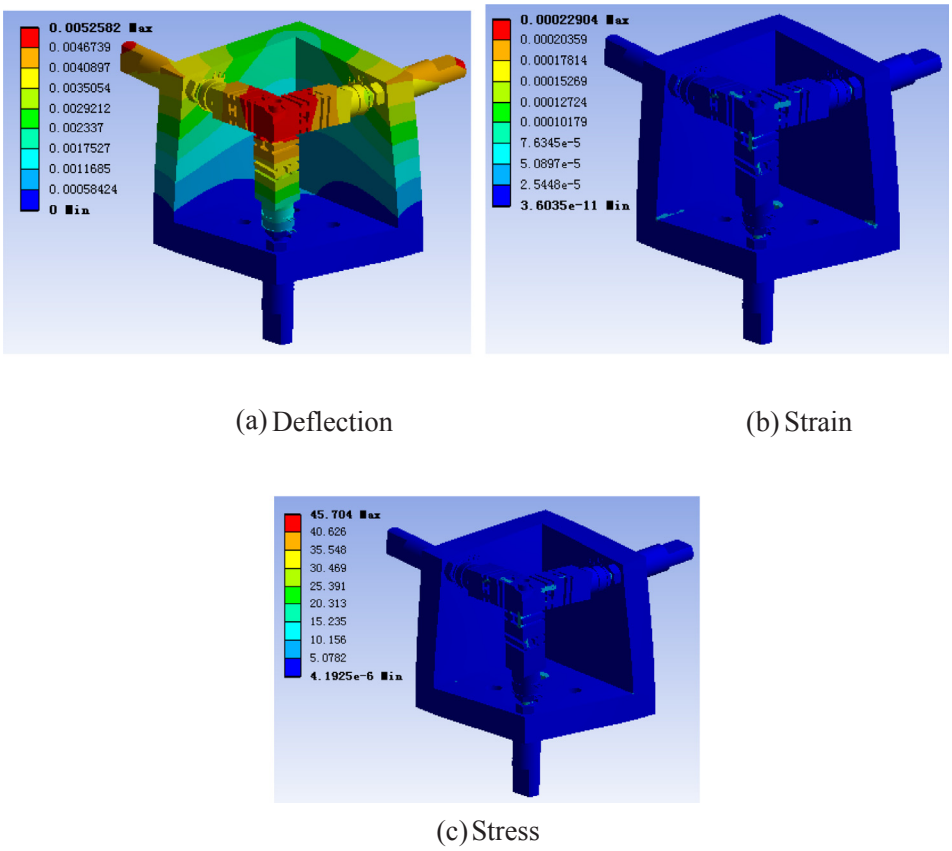

(a) Deflection (b) Strain

(c) Stress

Fig. 11. The results of FEA simulation with static force.

the same. The vibration amplitudes of 3D EVC mechanism reach their maximum value at frequencies of 3.4 kHz, 7.7 kHz, 37.2 kHz and 44.2 kHz corresponding to the three respective modal responses. These resonant frequencies of the designed 3D EVC mechanism will be compared and analysed based on the actual test of the developed 3D EVC mechanism in the following Section 4.

4. Experiments and verification

4.1. Experimental setup

A test system for the performance evaluation of the vibration cutting tool is shown in Fig. 13(a). This system consists of a personal computer, high-speed digital-to-analog converter, high-voltage amplifier, and capacitive displacement sensor. The PC provides the machine interface used for performance evaluation, and the high-speed digital-to-analog converter provides the sinusoidal voltage input to the tool to produce its fast motion. The high-voltage amplifier amplifies the input voltage from the digital-to-analog converter and drives the three piezoelectric actuators. The motion of the vibrating tool in each direction is measured by the capacitive displacement sensors, as shown in Fig. 13(b). The range and resolution of the capacitive displacement sensors are ± 50 μm and 10 nm, and the bandwidth is 100 kHz. Therefore, the elliptical vibration shapes of the tool in space can be measured. The test process is as follows. The signals are generated by Data Acquisition Card which is programmed by LABVIEW on PC, then amplified by the power amplifier (PZD350A) which has 0 to ± 350 V bipolar output. The two Langevin transducers are excited by the outputs of the amplifier. The displacements of the tool tip are measured by the Micro Sense capacitance sensors (5300) and processed by the Data Acquisition Card. The displacement data are shown in real time by the LABVIEW and recorded as LVM files in PC for post processing.

A number of test experiments about frequency response, phase difference effect on output displacement and the generated elliptical loci are conducted to examine the characteristics of the developed 3D ultrasonic EVC mechanism using the established test system. The actual measured results is also compared to the results from FEA simulation on the established models of the developed 3D ultrasonic EVC mechanism. The comparison analysis from test experiments and FEA simulation are described to verify the correctness of the established models of 3D ultrasonic EVC mechanism in Sections 4.2, 4.3 and 4.4. In order to reduce external disturbances on sensing and measurement system, a new port optical table is used to mount the 3D ultrasonic EVC mechanism.

4.2. Frequency response test and comparison

The resonant frequency is an important characteristic of the developed 3D ultrasonic EVC mechanism. The frequency sweep test is first performed to identify the resonant frequencies of 3D ultrasonic EVC mechanism. The results are compared with simulation results. The amplitudes of sinusoidal excitation signals applied on the PZT in test experiment are 350 V with a 0° phase difference between the signals; and the frequency is swept from 0 to 60 kHz with a step size of 200 Hz. The vibration amplitudes (output displacement) in three directions are measured at the tool tip of 3D ultrasonic EVC mechanism by capacitance sensors at a sampling frequency of 100 kHz using test system shown in Fig. 13. The measured vibration amplitudes (output displacement) are also recorded and analyzed and also plotted in Figs. 14–16 in three directions. FEA simulation results about vibration amplitudes (output displacement) are also plotted in Figs. 14–16 in three directions. Thus, the comparisons of frequency response and resonant frequency between FEA simulation results and measured results are shown in Figs. 14–16 in three directions. The comparisons of resonant frequency and error between FEA simulation results and

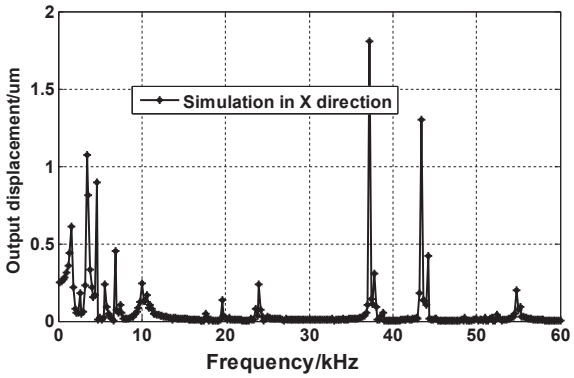

(a) Frequency response in X-direction

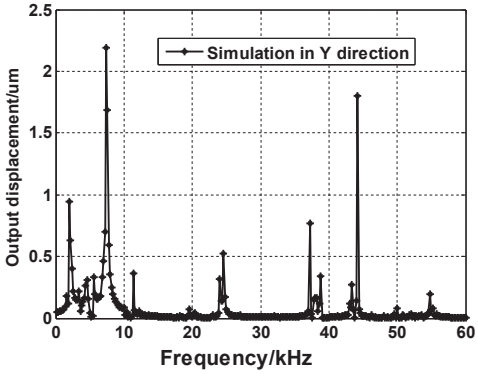

(b) Frequency response in Y-direction

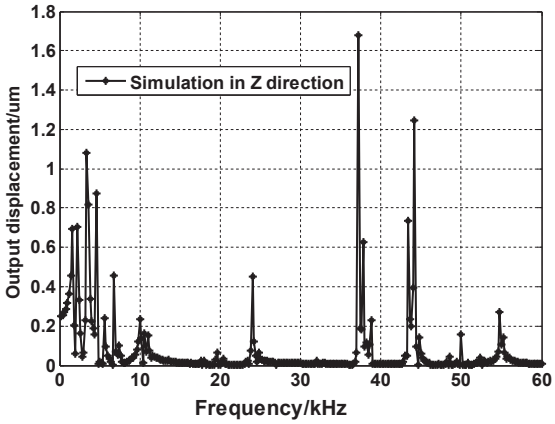

(c) Frequency response in Z-direction

Fig. 12. Influence of frequency on the amplitude in three directions.

measured results under different order are shown in Tables 2–4.

The comparison of frequency response between FEA simulation and measured results in X axis are shown in Fig. 14(a) and the resonant frequencies of the physical device basically consistent with the simulation results but a little deviation from the first order to the fourth order from Fig. 14(a). Fig. 14(b) gives the comparison of resonance frequency between FEA simulation and measured results under different orders and shows that there are little deviation between the actual measurement experiment and FEA simulation results. The comparison of the detailed resonance frequency and error between FEA simulation and actual measurement experiment in X axis is shown in Table 2. It can be seen from Table 2 that there exists the maximum error −23.38% in the third order and the minimum error 1.14% in the fourth order with the actual measured resonant frequency 44.5 kHz between FEA simulation and measured results.

The comparison of frequency response between FEA simulation and measured results in Y axis are shown in Fig. 15 and the relative error of resonance frequency between FEA simulation and measured results are listed in Table 3 from the first order to fourth order. It can be seen from the Fig. 15 and Table 3 that the resonance frequencies of the physical device basically consistent with the simulation results but a little deviation from the first order to the fourth order and the maximum relative error is 11.2% in the second order with simulation resonant frequency 25 kHz and the minimum relative error is 0.23% in the fourth order with the actual measured resonant frequency 44.1 kHz.

The comparison of frequency response between FEA simulation and measured results in Z axis are shown in Fig. 16 and the relative error of resonance frequency between simulation results and experiment results are listed in Table 4 from the first order to fourth order. The results show from Fig. 16 and Table 4 that the resonance frequencies of the

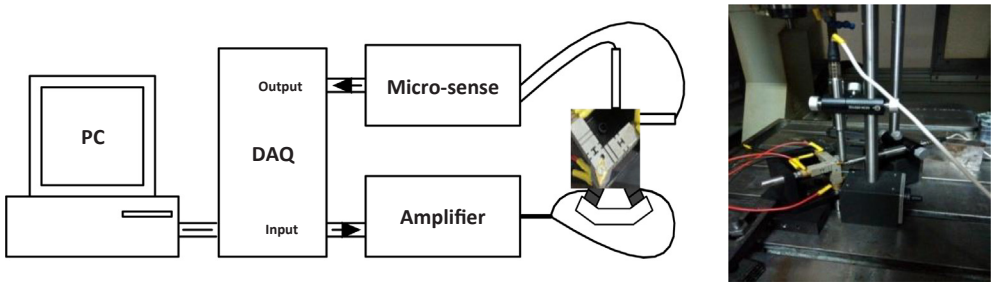

(a) Test system (b) Experimental process

Fig. 13. Experimental condition.

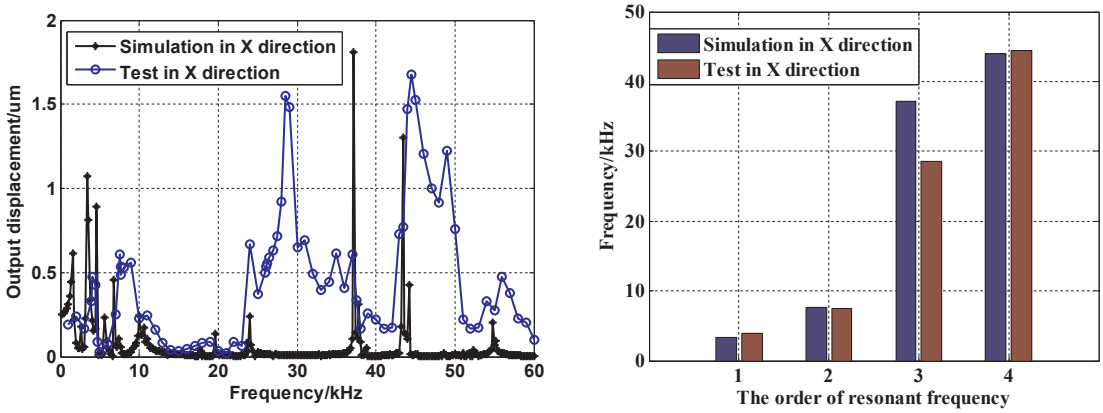

(a) Comparison of frequency response (b) Comparison of resonant frequency

Fig. 14. The comparisons between FEA simulation and measured results in X axis.

physical device basically consistent with the simulation results but a little deviation from the first order to the fourth order and the maximum relative error is 17.65% in the first order of resonance frequency with simulation resonant frequency 3.4 kHz and the minimum relative error is 0.6% in the fourth order with the actual measured resonant frequency 44.5 kHz.

It can be seen from the comparison analysis of Figs. 14–16 and Tables 2–4 that the trends of FEA simulation and measured results are basically in accordance with each other but exists a certain difference between the simulation and experimental results. The experimental results verify most of the simulation predictions with an acceptable level of deviation. The discrepancy is resulted from the following reasons: (1) the actual fixture structure and the non-perfect fixed boundary condition will possibly contribute to the discrepancy; (2) The PZT's calibration coefficient error in actual measurement experiment may cause the discrepancy. (3) There exits little cross-talk/couplings between the motion directions in the developed 3D ultrasonic EVC mechanism and this will be one of reasons, which lead to the discrepancy. The error comparisons of resonant frequency show that the fourth order resonant frequency has the minimum error 1.14%, 0.23% and 0.6% in X axis, Y axis and Z axis between FEA simulation and actual measurement results. At the same time, the fourth order resonant frequencies in X axis, Y axis and Z axis are almost same no matter for FEA simulation results or for the actual measured results. Thus the fourth order resonant frequency is best choice for the develop 3D ultrasonic EVC mechanism and the resonant frequency 44.5 kHz of the fourth order from the actual measured results is calibrated as the output resonant frequency of 3D ultrasonic EVC mechanism. The frequency is large enough for successful operation of the tool in machining experiment by using the established 3D ultrasonic EVC mechanism.

4.3. Comparison between the actual and theoretical amplification ratios

In order to verify the correctness of amplification ratio model and obtain the actual amplification ratio, the actual output displacement of peak-to-peak amplitudes of the designed 3D ultrasonic EVC mechanism at 44.5 kHz are measured. The measured peak-to-peak amplitudes of the designed 3D ultrasonic EVC mechanism at 44.5 kHz are respectively 3.52 μm, 3.34 μm and 3. 50 μm in X axis, Y axis, and Z axis direction.

The displacement of PZT piezoelectric ceramics using in the developed 3D ultrasonic EVC mechanism can be calculated by the following formula:

$$\Delta L = nd_{33}U_3 \tag{17}$$

where n is the number of the piezoelectric ceramics, d_{33} is the piezoelectric coefficient of the thickness and thick deformation of piezoelectric ceramics, and U_3 refers to the amplitude of the excitation voltage.

In actual 3D EVC mechansim, piezoelectric actuator takes four piezoelectric ceramics and piezoelectric coefficient of piezoelectric ceramics d_{33} is 260 and the the excitation voltage is 350 V. Thus the calculated displacement of PZT piezoelectric ceramics is 0.364 μm and the actual amplification ratio of the designed 3D ultrasonic EVC mechanism in three directions can be calculated. The amplification ratio

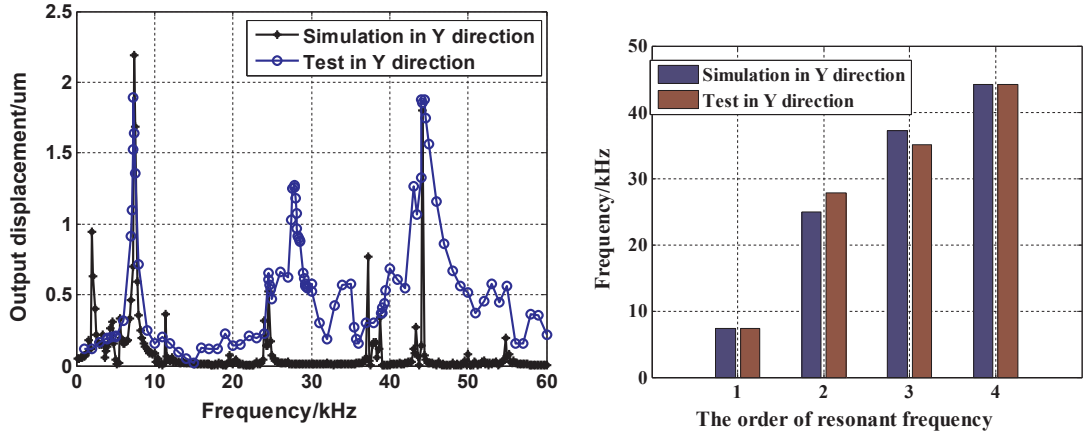

(a) Comparison of frequency response (b) Comparison of resonant frequency

Fig. 15. The comparisons between FEA simulation and measured results in Y axis.

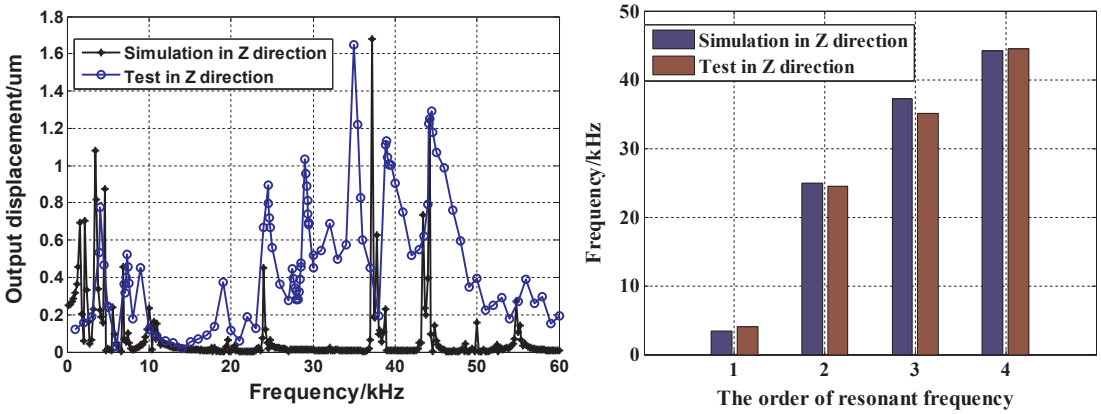

(a) Comparison of frequency response (b) Comparison of resonant frequency

Fig. 16. The comparisons between FEA simulation and measured results in Z axis.

Table 2
The comparisons of resonant frequency and error between FEA simulation and measured results in X axis.

Order	The first order	The second order	The third order	The fourth order
Simulation (kHz)	3.4	7.7	37.2	44
Experiment (kHz)	3.9	7.5	28.5	44.5
Error (%)	14.7%	−2.59%	−23.38%	1.14%

Table 3
The comparisons of resonant frequency and error between FEA simulation and measured results in Y axis.

Order	The first order	The second order	The third order	The fourth order
Simulation (kHz)	7.4	25	37.2	44.2
Experiment (kHz)	7.3	27.8	35	44.1
Error (%)	−1.35%	11.2%	−5.91%	−0.23%

Table 4
The comparisons of resonant frequency and error between FEA simulation and measured results in Z axis.

Order	The first order	The second order	The third order	The fourth order
Simulation (kHz)	3.4	24	37.2	44.2
Experiment (kHz)	4	24.5	35	44.5
Error (%)	17.65%	2.08%	−5.91%	0.6%

Table 5
The comparison of the theoretical and actual amplification ratios.

Amplification ratio	Theoretical calculation (μm)	The actual measurement (μm)	Error (%)
The X direction	4.814	4.835	0.4
The Y direction	4.814	4.588	4.6
The Z direction	4.814	4.808	0.1

from theoretical calculation and actual measurement of the designed 3D ultrasonic EVC mechanism in three directions is shown in Table 5.

It can be seen from Table 5 that there exist some discrepancies between the theoretical and actual amplification ratios of the designed 3D ultrasonic EVC mechanism in three directions. The discrepancies are equal to and less than 5%. The discrepancies are contributed to the differences between the physical properties of materials and the used material properties of the established theoretical models of amplification ratio. Besides, the manufactured error of 3D ultrasonic EVC mechanism and the rigging error are also the reason for these differences. The comparisons show that the established theoretical model of amplification ratio for the developed 3D ultrasonic EVC mechanism is satisfactory and can be used to guide the design of 3D ultrasonic EVC mechanism.

4.4. Excitation phase difference tests

The phase differences in the excitation signals have an effect on the generated elliptical locus of the tool tip, which can be described by the amplitudes and direction of the generated elliptical loci. The direction of the elliptical locus at the tool tip has important influence in EVC and the generated elliptical vibration locus with clockwise direction is suitable for the actual EVC machining. The elliptical trajectories of the 3D ultrasonic EVC mechanism are evaluated for different phase angles at the selected resonant frequency. The amplitudes of sinusoidal excitation signals are kept at 350 V while the phase difference is varied from 0° to 360° in 15° increments. Experimental tests and simulation for this effect are conducted. Fig. 18 shows the comparison between experimental and simulated amplitudes under different phase differences in one cycle along X axis, Y axis and Z axis. Blue lines in Fig. 17 express the experimental results under the effect of the phase differences, while black lines depict the corresponding simulation results. It can be seen from the Fig. 17(a) that the amplitude of the generated elliptical locus at the tool tip in the X-direction decrease with increases of the phase difference from 0° to 220° and increase for phase differences from 220° to 360°. The amplitudes are nearly the same for both the simulation and experimental results for a phase difference of 0° as seen in Fig. 17(a). The maximal amplitudes in the X-direction are achieved for a phase difference of 0°, while the minimal amplitudes at a phase difference of 220°.

Similar trends in the amplitude can also be observed in the Y-direction (Fig. 17(b)). The amplitudes of the generated elliptical locus at tool tip in the Y-direction decrease with the increase of the phase difference from 0° to 105° and increase for phase differences from 105° to 360°. The maximal amplitudes in the Y direction are achieved for phase difference of 0°. The minimal amplitude occurs for a phase difference of 105°.

The Z-direction, Fig. 17(c), exhibits identical behavioral trend, i.e., the amplitudes of the generated locus decrease with the increases of the phase difference from 0° to 200° and increase with for a phase difference from 200° to 360°. Again, the amplitudes are nearly the same for the simulation and experimental results for a phase difference of 200°. The maximal amplitudes in the Z-direction are achieved for a phase difference of 0°, while the minimal amplitudes for a phase difference of

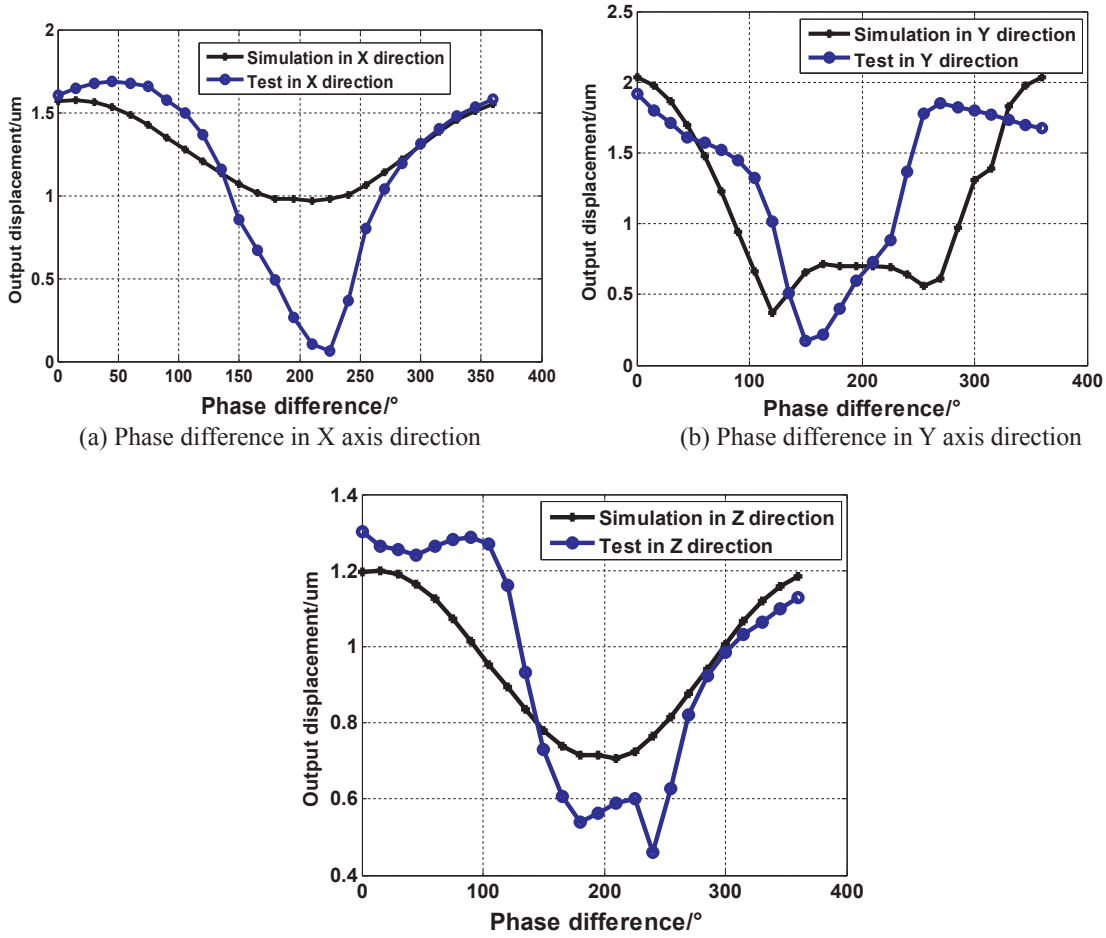

(a) Phase difference in X axis direction

(b) Phase difference in Y axis direction

(c) Phase difference in Z axis direction

Fig. 17. Excitation phase difference of 3D ultrasonic EVC in three directions.

200°.

In terms of the amplitudes in the three directions in the elliptical trajectory of the tool tip, as shown in Fig. 17, the trend of the amplitude variation in the simulation matches the experimental data well with small differences. These differences may be induced by the assemble precision of the 3D ultrasonic EVC mechanism.

The actual elliptical loci of the tool tip for phase differences ranging from 0° to 360° in 15° increments are also measured while the amplitudes and frequency of sinusoidal excitation signals are kept at 350 V and at 44.5 kHz. The actual measured results show the effect of the phase difference on the direction of the tool's trajectory. For each phase difference, the measured data are used to fit an elliptical locus in space in Matlab software. Fig. 18(a), (b), (c), (d) and (e) illustrate the actual measured elliptical vibration locus with phase difference 0°, 60°, 120°, 240°and 300°, respectively. The red arrows in Fig. 18 denote the direction of the generated elliptical vibration locus. The results in Fig. 18 show that the elliptical loci can be generated based on the designed 3D ultrasonic EVC mechanism in 3D space and that loci with well-defined profiles can be generated. It can be also seen from Fig. 18 that the developed 3D ultrasonic EVC mechanism can generate and realize the arbitrary elliptical vibration locus in space and the orientation and amplitude of the elliptical vibration locus varies with the change of the phase difference. Thus, the proposed 3D ultrasonic EVC mechanism can adjust the generated elliptical vibration locus by changing the input phase difference for fabricating the complicated micro/nano-structured surface under ultrasonic frequency 44.5 kHz.

4.5. Discussion

The above simulation and experiment results show that the established 3D ultrasonic EVC mechanism can be used to conduct the micro/nano-structured surface machining. The resonant frequency, excitation phase difference and the maximum amplitude of the developed 3D ultrasonic EVC mechanism can be regarded as an indicator of machining performance to predict the variation range of the machined micro/nano-structured surface. With three-phase sinusoidal driving excitation at 350 V at a frequency of 44.5 kHz, the developed prototype device achieved a 3D elliptical vibration. At an ultrasonic frequency of 44.5 kHz, the relative errors between simulation result and experimental result are respectively 1.14%, −0.23% and 0.6% in X axis, Y axis and Z axis. That is a little difference for simulation result and experimental result. Excitation phase difference tests show that the maximum amplitudes in X axis, Y axis and Z axis is achieved at phase difference 0°, and the minim amplitudes is achieved at phase difference 200°. The measured actual elliptical vibration locus show that the proposed 3D ultrasonic EVC mechanism can generate the different 3D elliptical vibration locus with the change of phase difference. The test experiments indicate that the performance of the developed 3D EVC device is satisfactory.

5. Conclusions

An innovative decoupled 3D ultrasonic EVC mechanism is proposed in the form of a compliant parallel mechanism in the paper. The related kinematics, amplification ratios and resonant frequencies of 3D

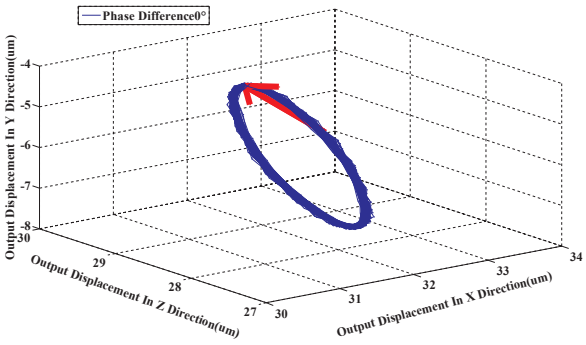

(a) Phase difference 0°

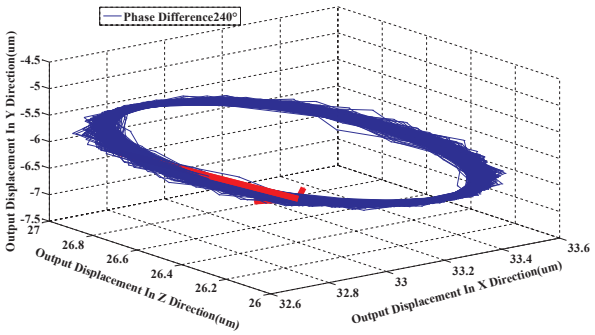

(d) Phase difference 240°

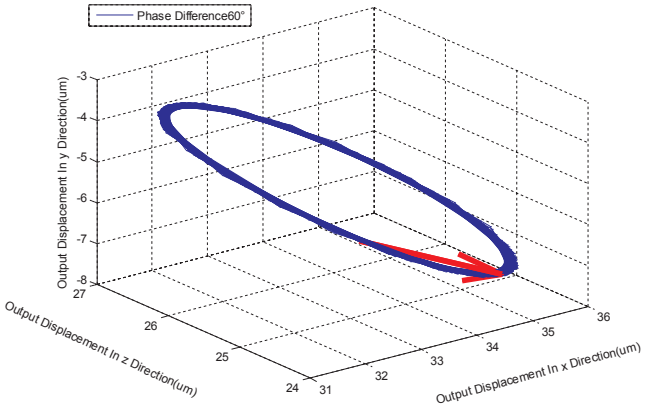

(b) Phase difference 60°

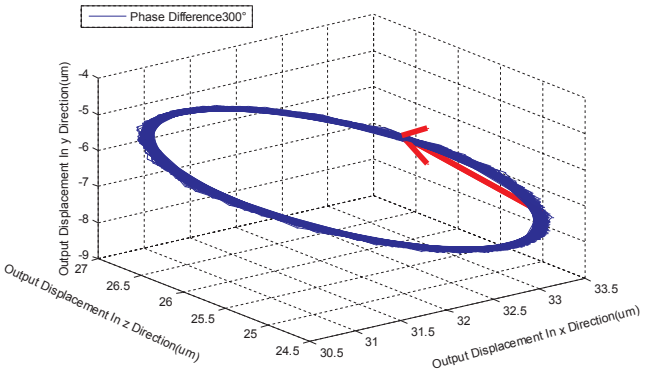

(e) Phase difference 300°

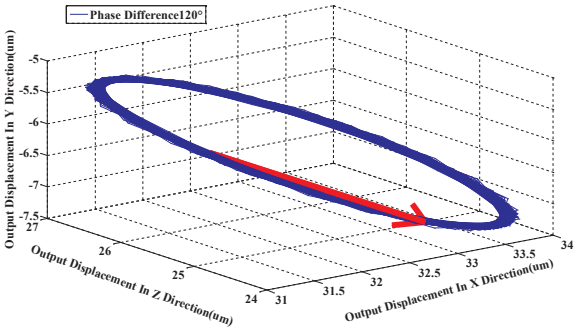

(c) Phase difference 120°

Fig. 18. The elliptical trajectory under different phase difference.

ultrasonic EVC mechanism are analytically modeled. Based on the above analysis, a prototype device is fabricated, and then its vibration characteristics are evaluated. The following is a summary of findings from the present work:

- The proposed innovative decoupled 3D ultrasonic EVC mechanism is designed to be capable of generating uniformly magnified output displacement in three directions by using orthogonal layout and includes multi-axis flexure hinge structure with three orthogonal sub chains, three piezoelectric actuators, three preload and adjust bi-nut structures and fixed platform.
- The 3D elliptical locus is obtained by the designed 3-DOF multi-axis flexure hinge structure with three orthogonal sub chains. The triangular amplification principles and three same orthogonal sub chains based on compliant parallel mechanism are used to establish the multi-axis flexure hinge mechanism with 3-DOF in order to improve the output properties of 3D ultrasonic EVC mechanism.
- The decoupling properties of 3D ultrasonic EVC mechanism are analyzed based on the established multi-axis flexure hinge mechanism by considering motion influence of other sub chains. Compared to the input of current sub chain, the motion of other sub chains have almost no effect on the input of current sub chain.
- The kinematics and amplification ratios of the proposed 3D ultrasonic EVC mechanism are analytically modeled based on the energy conservation law and triangular amplification principles and the theoretical output of the proposed 3D ultrasonic EVC mechanism can be obtained by the established kinematics model.
- The frequency responses of the proposed 3D ultrasonic EVC

mechanism are simulated by using FEA. Based on the above analysis results, a prototype device is fabricated, and then its vibration characteristics are evaluated by using the established test system.

- With three-phase sinusoidal driving voltages of 350 V at an ultrasonic frequency of 44.5 kHz, the developed prototype apparatus achieved a 3D elliptical vibration with the peak-to-peak amplitudes are respectively 3.52 μm, 3.34 μm and 3. 50 μm in X axis, Y axis, and Z axis. The test experiments indicate that the performance of the developed 3D ultrasonic EVC mechanism is satisfactory.

Acknowledgements

This paper was funded by the National Natural Science Foundation of China under grants No 51675277 and High Level Talents Project of “Six Talents Summit” in Jiangsu Province of China under grants No GDZB-011.

References

[1] D.E. Brehl, T.A. Dow, Review of vibration-assisted machining, Precis. Eng. 32 (3) (2008) 153–172.
[2] C. Ma, E. Shamoto, T. Moriwaki, Y. Zhang, L. Wang, Suppression of burrs in turning with ultrasonic elliptical vibration cutting, Int. J. Mach. Tools Manuf. 45 (11) (2005) 1295–1300.
[3] J. Zhang, T. Cui, C. Ge, Y. Sui, H. Yang, Review of micro/nano machining by utilizing elliptical vibration cutting, Int. J. Mach. Tools Manuf. 106 (2016) 109–126.
[4] Z.W. Zhu, S. To, K.F. Ehmann, G. Xiao, W.L. Zhu, A novel diamond micro-/nano-machining process for the generation of hierarchical micro-/nano-structures, J. Micromech. Microeng. 26 (3) (2016) 035009.
[5] Z.W. Zhu, S. To, W.L. Zhu, P. Huang, X. Zhou, Cutting forces in fast-/slow tool servo diamond turning of micro-structured surfaces, Int. J. Mach. Tools Manuf. 136 (2019) 62–75.
[6] W.L. Zhu, Z. Zhu, Y. He, K.F. Ehmann, B. Ju, S. Li, Development of a novel 2d vibration-assisted compliant cutting system for surface texturing, IEEE/ASME Trans. Mechatron. 22 (4) (2017) 1796–1806.
[7] N. Suzuki, H. Yokoi, E. Shamoto, Micro/nano sculpturing of hardened steel by controlling vibration amplitude in elliptical vibration cutting, Precis. Eng. 35 (1) (2011) 44–50.
[8] J.G. Zhang, N. Suzuki, Y. Wang, E. Shamoto, Ultra-precision nano-structure fabrication by amplitude control sculpturing method in elliptical vibration cutting, Precis. Eng. 39 (2015) 86–99.
[9] R. Gandhi, D. Sebastian, S. Basu, J.B. Mann, P. Iglesias, C. Saldana, Surfaces by vibration/modulation-assisted texturing for tribological applications, Int. J. Adv. Manuf. Technol. 85 (1–4) (2016) 909–920.
[10] E. Brinksmeier, R. Glabe, J. Osmera, Ultra-precision diamond cutting of steel molds, CIRP Ann. Manuf. Technol. 55 (1) (2006) 551–554.
[11] E. Shamoto, N. Suzuki, E. Tsuchiy, Y. Hori, H. Inagaki, K. Yoshino, Development of 3 DOF ultrasonic vibration tool for elliptical vibration cutting of sculptured surfaces, CIRP Ann. Manuf. Technol. 54 (1) (2005) 321–324.
[12] J.Q. Lin, X.Q. Zhou, Y.C. Li, Tool path generation for fabricating optical freeform surfaces by non-resonant 3D elliptical vibration cutting, Proc. Instit. Mech. Eng. Part C: J. Mech. Eng. Sci. 228 (7) (2014) 1208–1222.
[13] G.D. Kim, B.G. Loh, Direct machining of micro patterns on nickel alloy and mold steel by vibration assisted cutting, Int. J. Precis. Eng. Manuf. 12 (4) (2011) 583–588.
[14] G.D. Kim, B.G. Loh, Machining of micro-channels and pyramid patterns using elliptical vibration cutting, Int. J. Adv. Manuf. Technol. 49 (9) (2010) 961–968.
[15] P. Guo, K.F. Ehmann, Development of a tertiary motion generator for elliptical vibration texturing, Precis. Eng. 37 (2) (2013) 364–371.
[16] X. Zhang, A.S. Kumar, M. Rahman, C. Nath, K. Liu, Experimental study on ultrasonic elliptical vibration cutting of hardened steel using PCD tools, J. Mater. Process. Technol. 211 (11) (2011) 1701–1709.
[17] C. Zhang, K.F. Ehmann, Y. Li, Analysis of cutting forces in the ultrasonic elliptical vibration-assisted micro-groove turning process, Int. J. Adv. Manuf. Technol. 78 (1) (2015) 139–152.
[18] Y. Li, Q. Xu, A totally decoupled piezo-driven xyz flexure parallel micropositioning stage for micro/nanomanipulation, IEEE Trans. Autom. Sci. Eng. 8 (2) (2011) 265–279.
[19] G. Hao, H. Li, R. Kavanagh, Design of decoupled, compact, and monolithic spatial translational compliant parallel manipulators based on the position space concept, Proc. IMechE, Part C: J. Mech. Eng. Sci. 230 (3) (2016) 367–378.
[20] H. Tang, Y. Li, Development and active disturbance rejection control of a compliant micro-/nanopositioning piezostage with dual mode, IEEE Trans. Ind. Electron. 61 (3) (2014) 1475–1492.
[21] G. Hao, Towards the design of monolithic decoupled XYZ compliant parallel mechanisms for multi-function applications, Mech. Sci. 4 (2013) 291–302.
[22] H. Li, G. Hao, A constraint and position identification (CPI) approach for the synthesis of decoupled spatial translational compliant parallel manipulators, Mech. Mach. Theory 90 (2015) 59–83.
[23] H.W. Ma, S.M. Yao, L.Q. Wang, Z. Zhong, Analysis of the displacement amplification ratio of bridge-type flexure hinge, Sens. Actuat. A: Phys. 132 (2006) 730–736.
[24] Y.K. Yong, T.F. Lu, Kinetostatic modelling of 3-RRR compliant micro-motion stages with flexurehinges, Mech. Mach. Theory 44 (2009) 1156–1175.
[25] Q. Liang, D. Zhang, Z. Chi, Q. Song, Y. Ge, Y. Ge, Six-DOF micro-manipulator based on compliant parallel mechanism with integrated force sensor, Rob. Comput. Integr. Manuf. 27 (2011) 124–134.
[26] Z.W. Zhu, S. To, W.L. Zhu, Y.M. Li, P. Huang, Optimum design of a piezo-actuated tri-axial compliant mechanism for nano-cutting, IEEE Trans. Ind. Electron. (2017), https://doi.org/10.1109/TIE.2017.2787592.
[27] G. Hao, H. Li, Design of 3-legged xyz compliant parallel manipulators with minimised parasitic rotations, Robotica 33 (04) (2015) 787–806.